Evaluation of CRISPR/Cas9 exon-skipping vector for choroideremia using human induced pluripotent stem cell-derived RPE

Toshiro Iwagawa[1,2], **Hiroki Masumoto**[3,4], **Hitoshi Tabuchi**[4,5], **Kenzaburo Tani**[6], **Bruce R. Conklin**[7,8], **Sumiko Watanabe**[1,2]

[1]Division of Molecular and Developmental Biology, Institute of Medical Science, University of Tokyo, Tokyo, Japan

[2]Department of Retinal Biology and Pathology, University of Tokyo Hospital, University of Tokyo, Tokyo, Japan

[3]Xeno Hoc, inc

[4]Department of Ophthalmology, Tsukazaki Hospital, Hyogo, Japan

[5]Department of Technology and Design Thinking for Medicine, Hiroshima University, Hiroshima, Japan

[6]Laboratory of ALA Advanced Medical Research, Institute for quantitative Biosciences, University of Tokyo, Tokyo, Japan

[7]Gladstone Institutes, San Francisco, CA, USA.

[8]Departments of Medicine, Ophthalmology & Cellular and Molecular Pharmacology University of California, San Francisco, CA, United States, USA.

Abstract

Background: Exon-skipping is a powerful genetic tool, especially when delivering genes using an AAV-mediated full-length gene supplementation strategy is difficult due to large length of genes. Here, we used engineered human induced pluripotent stem cells (hiPSCs) and artificial intelligence (AI) to evaluate clustered regularly interspaced short palindromic repeats (CRISPR)/CRISPR associated protein 9 (Cas9)-based exon-skipping vectors targeting genes of the retinal pigment epithelium (RPE). The model system was choroideremia; this is an X-linked inherited retinal disease caused by mutation of the *CHM* gene.

Methods: We explored whether AI detected differentiation of human *OTX2*, *PAX6*, and *MITF* (hOPM) cells, in which *OTX2*, *PAX6*, and *MITF* expression were induced by doxycycline

Corresponding author: Sumiko Watanabe (Current affiliation), Department of Retinal Biology and Pathology, Graduate School of Medicine, The University of Tokyo, 7-3-1 Hongo, Bunkyo-ku, Tokyo 113-8655, Japan, Phone : 81-3-5800-9008, sumiko@g.ecc.u-tokyo.ac.jp.

Conflict of Interest Statement: The authors have none of conflict of interest on this work.

treatment, into RPE. Plasmid encoding *CHM* exon-skipping modules targeting the splice donor sites of exons 6, was constructed. A clonal hOPM cell line with a frameshift mutation in exon 6 was generated and differentiated into RPE. *CHM* exon 6-skipping was induced, and the effects of skipping on phagocytic activity, cell death, and prenylation of Rab small GTPase (RAB) were evaluated using flow cytometry, an *in vitro* prenylation assay, and Western blotting.

Results: AI-based evaluation of RPE differentiation was successful. RPE cells with a frameshift mutation in exon 6 showed increased cell death, reduced phagocytic activity, and increased cytosolic unprenylated RABs only when oxidative stress was in play. The latter two phenotypes were partially rescued by exon 6-skipping of *CHM*.

Conclusions: *CHM* exon 6-skipping contributed to RPE phagocytosis probably by increasing RAB38 prenylation under oxidative stress.

Graphical Abstract
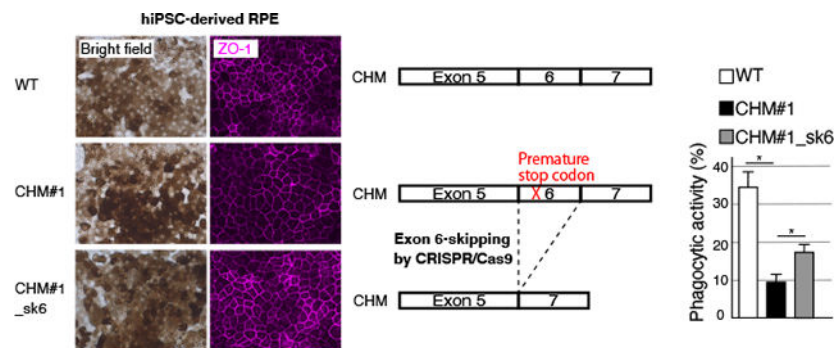
RPE cells derived from hiPSCs with a frameshift mutation in exon 6 of *CHM* showed reduced phagocytic activity under oxidative stress.

The phenotype was partially rescued by exon 6-skipping induced by the CRISPR/Cas9 system.

Keywords

CHM; choroideremia; exon-skipping; CRISPR/Cas9; hiPSC; RPE

Introduction

The retinal pigment epithelium (RPE) is a monolayer of cells adjacent to the photoreceptor layer. The RPE plays a pivotal role in vision, maintaining photoreceptor health and function principally by phagocytosis of shed photoreceptor outer-segments and recycling visual molecules [1]. If the RPE dies or becomes dysfunctional, the photoreceptors degenerate, and vision is lost. Inherited retinal diseases (IRDs) such as retinitis pigmentosa (RP) trigger photoreceptor cell degeneration. In addition to the photoreceptor specific genes, several RPE specific genes, such as *RPE65*, had been identified to be causal of IRD by their mutations [2]. Therefore, RPE is being sought to be therapeutic targets [3], and several treatments are under development. A recombinant adeno-associated virus (rAAV)-based gene therapy for biallelic *RPE65* mutation-associated retinal dystrophy was approved by the U.S. Food & Drug Administration in 2017; this was the first such therapy approved

worldwide [4,5]. Although rAAV-mediated gene transfer is promising, the limitations include the development of neutralizing antibodies against the AAV capsid proteins [6] and the small packaging capacity (less than 5 kb). Thus, it is difficult to deliver large genes such as *EYS* and *MYO7A* to retina or RPE.

When seeking to develop therapeutic tools, manipulation of the human RPE is essential. It is important to understand the pathophysiology in great detail and to screen the actions of pharmacological drugs. The major sources of human RPE cells are embryonic stem cells (ESCs) and human induced pluripotent stem cells (hiPSCs) [7,8]; several protocols that cause ESCs/iPSCs to differentiate into RPE have been reported [9]. Accurate evaluation of differentiation is critical. Here, we established a rapid and simple evaluation platform using clustered regularly interspaced short palindromic repeats (CRISPR)/CRISPR associated protein 9 (Cas9)-based exon-skipping of hiPSCs. We chose choroideremia (*CHM*) as the model system.

Choroideremia is an X-linked IRD characterized by degeneration of the choroid, retina, and RPE. Choroideremia is caused by mutations in the *CHM* gene, which encodes Rab escort protein 1 (REP-1). About 30% of all mutations are nonsense mutations; at least one nonsense mutation has been identified in each exon [10]. CHM is essential for prenylation of Rab small GTPases (RABs) involved in secretion, phagocytosis and intracellular tracking [11]. In choroideremia patients, CHM dysfunction triggers the accumulation of unprenylated RABs, which are thought to be related to the degeneration of the RPE, retina, and choroid [12]. A gene therapy (provision of full-length CHM via rAAV transfection) is in phase III clinical trials [13,14].

Here, we studied a recently established hiPSC line, the human OTX2, PAX6, and MITF (hOPM) cell line [15]. In this line, expression of exogenous *OTX2*, *PAX6*, and *MITF*, which are inserted in the AAVS1 locus, is induced by doxycycline; RPE differentiation is then rapidly and effectively induced. We established a non-invasive artificial intelligence (AI)-based cell evaluation system. As *CHM* lies in the X-chromosome, we used only male hiPSCs because manipulation of only one *CHM* gene was required. Because the CRISPR/Cas9-mediated exon-skipping allows us of the endogenous promoter and removal of the unprenylated RABs, and would be a permanent therapy, we explored whether exon-skipping induced by CRISPR/Cas9 gene editing could serve as a choroideremia therapy. We established a clonal hOPM cell line with a frameshift mutation in exon 6 and differentiated into RPE. *CHM* exon 6-skipping was induced, and the effects of skipping on phagocytic activity, cell death, RAB prenylation, and RAB localization were evaluated.

Materials and Methods

hiPSC culture, the establishment of hOPM cell line, RPE differentiation, and induction of exon skipping using the CRISPR/Cas9 system

WTC11 cells [16] were cultured according to the protocol provided in the following site: https://labs.gladstone.org/conklin/protocols.html. The establishment of hOPM cell line and differentiation of hOPM into RPE were done following the previous report [15]. After reaching confluent on a 12 well plate coated with Matrigel (Coring, 356231), hOPM

cell lines were cultured with the RPEMM1 [15] without nicotinamide. After 7 weeks culture medium was changed to X-VIVO 10 (Lonza, 04-380Q). We confirmed doxycycline dependent differentiation of hOPM to RPE by morphological observation (Supplemental Fig. 1A) and gene expression (Supplemental Fig. 1B). To induce exon 6-skipping, hOPM RPE cells were transfected with plasmid described below by Neon Transfection System (ThermoFisher Scientific) and cultured for 7 weeks with X-VIVO 10. To induce oxidative stress, RPE cells were incubated with X-VIVO 10 containing 2 mM sodium iodate (Sigma Aldrich, S4007) for 1 day.

Genome edition using the CRISPR/Cas9 system and the establishment of clonal cell lines

The target site (Supplemental Table 1) of guide RNA (gRNA) was designed by using CRISPRdirect (https://crispr.dbcls.jp/). Oligo DNAs were hybridized and inserted into the *BbsI* sites of pSpCas9(BB)-2A-GFP (PX458, Addgene, 48138). To construct PX458 expressing Cas9 VQR variant (D1135V/R1335Q/T1337R), each mutation was introduced by an inverse PCR-based mutagenesis kit (Toyobo, SMK-101). hOPM cells were transfected with the plasmids by Neon Transfection System. After 2 days of culture, GFP-expressing cells were sorted by using FACSAria II (BD). For the establishment of clonal cell lines, 5E3 cells were seeded on a 6 well plate. Genomic PCR was carried out using PrimeSTAR GXL DNA polymerase (Takara, R050).

Reverse transcription and semi-quantitative or quantitative PCR (RT-qPCR), droplet digital PCR (ddPCR), immunocytochemistry

Total RNA was extracted using Sepasol RNA I Super G (Nacalai tesque, 09379) and cDNA was synthesized using ReverTra Ace (Toyobo, FSQ-301). Semi-quantitative PCR or qPCR was performed using PrimeSTAR GXL DNA polymerase or THUNDERBIRD SYBR qPCR Mix (Toyobo, QPS-101) and LightCycler 96 (Roche), respectively. The relative mRNA expression level was normalized by the expression level of *ACTB* and *GAPDH*. Quantitative ddPCR was carried out by using QX200 ddPCR System (BioRad) and ddPCR Supermix for Probes (BioRad, 1863024). The same amounts of cDNA were used for templates. Primer sequences are available in Supplemental Table 1.

RPE cells derived from hOPM cell lines were seeded on a chamber slide glass (Corning, 354118) coated with Matrigel. Immunostaining was done as previously described [17] using antibodies indicated in Supplemental Table 2. Nuclei were visualized with 4', 6-diamidino-2-phenylindole dihydrochloride (DAPI). Fluorescence images were obtained using Zeiss Axio Imager M2 (ZEISS).

Phagocytosis assay

Porcine eyes were obtained from Tokyo Shibaura Zouki, and photoreceptor outer segment (POS) was prepared as previous reported [18]. Fluoresbrite YG Microspheres latex beads (Polysciences, 17154-10) were mixed with 1.5 mg of POS in DMEM medium with 2.5% sucrose and rotated at room temperature for 1 hour for opsonization of latex beads with POS to enhance phagocytic activity [19]. After washing with 0.9% NaCl solution, beads were resuspended with X-VIVO 10 containing 30% fetal bovine serum (FBS) and incubated with RPE cells which were preincubated with X-VIVO 10 containing 30% FBS for 1 hour to

prime cells [20]. After 24 hours of culture, RPE cells were resuspended with X-VIVO 10 containing propidium iodate and analyzed by using FACSAria II.

Building of neural network and training

We made a model based on VGG16 [21], which is a convolutional neural network model contains 5 blocks; convolutional layer, ReLU activation function, and Max pooling layer [22]. We used initial parameter of the 5 blocks by using results obtained by ImageNet training. Then, stacked information in the blocks were further stacked to 2-dimension. Finally, probability of each class was returned by the softmax formula.

Construction of an automated model to choose differentiated regions

We compared total non-pigmented (undiff) (1847 blocks), mix (1227 blocks) and pigmented (diff) blocks (1387 blocks) by the model, and cross-segregation of matrix was performed. We found that undiff and diff were identified about 80% accuracy, but lower accuracy was observed with mix blocks, which was predictable because mix contains mingled diff and undiff regions (Supplemental Fig. 2A). Only less than 50 % of accuracy was obtained with mix category (Supplemental Fig. 2A), that is predictable since the category contains both undiff and diff regions. Based on the results, we then generated a model to classify the blocks to diff and undiff automatically. We used undiff (322 blocks), diff (358 blocks) for building a model for automated classification of diff and undiff blocks. Since we used softmax formula, the output of the neural network model is total 1 probability i.e. {Diff:0;9, Undiff:0.1}. The differentiation classification model was applied to total 1907 blocks, and output is shown in Supplemental Fig. 2B. Then, based on the probability of judgement as "diff", we adjusted threshold to make Youden index as maximum. Judgement of either "mix" or "undiff" was also made by using the same method. The identification of "undiff", "mix", and "diff" patches was used for the judgement of the maturation of hOPM RPE cells, and mixed populations were used in the experiments for the evaluation of the effects of a *CHM* mutation and exon-skipping.

In vitro prenylation assay and Western Blotting

In vitro prenylation assay was performed following previously reports [23]. In brief, RPE cells were resuspended with cold prenylation buffer (25 mM HEPES pH 7.2, 50 mM NaCl, 2 mM $MgCl_2$, 2 mM DTE, 20 μM GDP) containing protease inhibitor cocktail (Nacalai tesque, 25955). After cellular debris was removed, supernatant was ultracentrifuged at 80,000 × rpm for 60 minutes at 4 °C. The supernatant was concentrated by using Amicon Ultra (Millipore, UFC200324) and used for *in vitro* prenylation assay or as cytoplasm fraction. The supernatant was incubated with 1 μM RabGGTase (JenaBioscience, PR-103), 1 μM REP-1 (JenaBioscience, PR-105), and 5 μM biotin-geranyl pyrophosphate (JenaBioscience, LI-105) for 6 hours at room temperature. Biotin-labeled RAB protein was detected by using streptavidin-HRP (Invitrogen, 434323) and Amersham Imager 600 (Cytiva). In Western blotting analysis of cytoplasm fraction, mouse IgG anti-ACTIN (Sigma aldrich, A4700), anti-RAB27A (Santa cruz, sc-81924), anti-RAB38 (Santa cruz, sc-390176), anti-REP-1 (Santa cruz, sc-23905) and HRP-linked anti-mouse IgG antibody (Cytiva, NA-9310) were used. The signal quantification was carried out by using ImageQuant TL (Cytiva).

Statistical analysis

Statistical analysis was done using Python Scipy (https://scipy.org/). The p-values were calculated Tukey's test as indicated in the figure legends by using R software (The R Foundation for Statistical Computing, Vienna, Austria).

Results

AI-based evaluation of cell differentiation into RPE

We established the hOPM cell line by introduction of the plasmids as previously described [15]. In the hOPM cell line, RPE differentiation is not homogeneous; pigmented and non-pigmented regions are intermingled (Fig. 1A). We first confirmed that *OTX2* and *MITF* were expressed only in pigmented cells (Fig. 1B), and the pigmented and non-pigmented regions are referred as "diff" and "undiff", respectively. We explored whether deep-learning could be used to identify the developmental transition into hiPSC-derived RPE. Photographs were taken using a conventional microscope (Nikon Eclipse, TE300) and camera (Nikon, D3300) (Fig. 1A), and then divided into small squares; an expert separated the pigmented and non-pigmented areas. The former were dark, the cells were hexagonal, and the cell edges were visible (Fig. 1A, C). Each "diff" block contains 7–8 hexagonal cells (Fig. 1D, E). Blocks with both "undiff" and "diff" regions were classified as mixed (Fig. 1D). The population of "diff" blocks increased linearly for 7 weeks, and was then maintained at about 30% of the total (Fig. 1F).

We examined whether "undiff", "mixed", and "diff" blocks could be separated by AI. K-fold cross validation (k = 5) was used to create a model based on the VGG16 convolutional neural network (CNN). Cross-segregation consistently afforded 70–80% accuracy in terms of "diff"/"undiff" separation at 4/5, 6/7, and 8/9 weeks (Tables 1–3). AI distinguished "diff" regions at these times with remarkable accuracy (> 99%) (Table 4).

AI-based identification of various developmental stages of hiPSC-derived RPE cells

Using a fresh culture, we took 10 photographs daily in weeks 1, 4, 8, and 13 after RPE differentiation commenced and prepared small blocks (14 × 21 blocks from one photo). "Diff"/"undiff" classification was based on the softmax model described in the Materials and Methods. Cross-validation revealed that the accuracy was 90–100% (data not shown). Then, we prepared a new series of photographs (the test data) and evaluated predictions of culture-weeks. The accuracy was very high in weeks 1, 4 and 8, but only about 50% in week 13 (Table 5), suggesting that later samples exhibited similar profiles. We used the system to confirm maturation of hiPSCs into RPE in the following experiments.

Construction of exon-skipping vectors and evaluation thereof in Y79 cells

We chose *CHM* as a model for evaluation of exon-skipping in hOPM cells. *CHM* mutations of the patients are found in most of coding regions of *CHM* (Supplemental Fig. 3A). As the numbers of nucleotides of exons 6, 9, and 10 are multiples of 3, the exon 6, 9, or 10 skipping is in-frame. We designed gRNAs targeting the splice acceptor (SA) or splice donor (SD) sites and found that Cas9 cut close to the SD sites of exons 6, 9, and 10 (Supplemental Fig. 3B). Before expressing the skipping vector in hOPM cells, we checked whether the

vector worked in a conventional cell line Y79 retinoblastoma line [24] for the first screen in various ways. After electroporation of the vector into Y79 cells, we sorted GFP-positive cells. The RT-PCR and droplet digital PCR (ddPCR) results indicated reduced expression of *CHM* mRNA containing exon 6, 9, or 10 and also induction of *CHM* mRNA synthesis in the absence of exon 6, 9, or 10 (Supplemental Fig. 4A, B); ddPCR quantitated the exon-skipping rate (Supplemental Fig. 4B). Decomposition (TIDE) assay [25] predicted high indel efficiency around the SD site of exon 6, 9, or 10 explaining the high level of *CHM* exon 6, 9, or 10-skipping (Supplemental Fig. 4C), meaning that the first screening using Y79 identified the promising vectors. We then focused on the hiPSC line.

CHM exon 6-skipping was associated with expression of truncated REP-1 in hiPSCs

Plasmids expressing Cas9, gRNA, and GFP were introduced to WTC11 cells, and RT-PCR of purified GFP-expressing cells revealed bands corresponding to *CHM*-encoding mRNA without the target exons (Fig. 2A). We confirmed exon-skipping by sequencing the RT-PCR products, and the genomic DNA regions around the target SD sites (Fig. 2A, B, Supplemental Fig. 3B). The molecular weights of the truncated REP-1 were as expected in all cases (Fig. 2C). REP-1 lacking exon 9 or 10 exhibited faint bands, but the expression level of REP-1 lacking exon 6 was much stronger (Fig. 2C). The result indicated that REP-1 lacking exon 6 is more stable than REP-1 lacking exon 9 or 10 and exon 6-skipping is more effective. Thus, we focused on *CHM* exon 6-skipping below.

CHM exon 6-skipping was induced in RPE cells with a frameshift mutation in that exon

We established a clonal hOPM cell line (CHM#1) with a 17-nt deletion in exon 6 and a premature stop codon (Fig. 3A). Plasmids expressing Cas9 and gRNA targeting the *CHM* exon 6 SD site (gCHM_Ex6SD) or control luciferase (gLuc) were introduced into CHM#1 RPE cells via electroporation. Immunocytochemistry confirmed the RPE differentiation; OTX2 and PAX6 were expressed in the nuclei, and ZO-1 in the cell membranes, of all three samples (Fig. 3B). We used the AI-based staging method to evaluate whether the mutation affected maturation of RPE cells over 14 weeks. AI judged that the cells are at 13 weeks of culture period among 1, 4, 8 and 13-week options with over 90% prediction in all three samples (Fig. 3C). This suggested that neither the frameshift mutation in *CHM* exon 6, nor *CHM* exon 6-skipping, adversely affected differentiation into an RPE.

Exon 6-skipping was confirmed in CHM#1_sk6 RPE cells (Fig. 3D). We found that the *CHM* mRNA level was reduced (compared to that in WT RPE cells) probably due to nonsense mediated decay in CHM#1 RPE cells, but this deficit was rescued in CHM#1_sk6 RPE cells (Fig. 3D). Finally, we examined REP-1 expression levels using Western blotting. In CHM#1 RPE cells, REP-1 expression was minimal (Fig. 3E); however, we observed truncated REP-1 expression in CHM#1_sk6 RPE cells (Fig. 3E). Because the REP-1 expression level in CHM#1_sk6 was not restored as the *CHM* mRNA level, REP-1 lacking exon 6 was likely unstable compared with full-length REP-1.

CHM exon 6-skipping rescued the reduced phagocytic activity of CHM#1 RPE cells under oxidative stress

We then evaluated phagocytic activity via flow cytometry. We observed no decrease in the percentage of FITC-positive cells among CHM#1 RPE cells (Supplemental Fig. 5). In addition, the cell death levels of CHM#1 RPE and control cells were comparable (Supplemental Fig. 5). Since *CHM* dysfunction is associated with high levels of oxidative stress, we employed sodium iodate, which induces oxidative stress to RPE cells [26,27]. In WT RPE cells, treatment with sodium iodate for 1 day decreased phagocytic activity and increased cell death (Supplemental Fig. 5 and Fig. 4A, B); both phenomena were accelerated in CHM#1 RPE cells (Fig. 4A, B). In CHM#1_sk6 RPE cells, although the level of (accelerated) cell death was the same as that of as CHM#1 RPE cells (Fig. 4B), the phagocytic activity was significantly restored (Fig. 4A). This suggested that REP-1 lacking exon 6 was partially functional and contributed to the phagocytic activity of RPE cells under oxidative stress conditions.

REP-1 lacking exon 6 is likely to contribute to prenylation of RAB38 but not RAB27A

REP-1 controls cellular RAB localizations via prenylation; we thus examined the prenylation status of RABs in RPE cells under oxidative stress using an *in vitro* prenylation assay, which labels unprenylated RABs with biotin. CHM#1 RPE cells showed significantly higher levels of unprenylated RABs than did WT RPE cells (Fig. 4C). The high levels of unprenylated RABs were maintained in CHM#1_sk6 RPE cells (Fig. 4C). Most RABs are prenylated and then localized to cellular membranes; unprenylated RABs reside in the cytosol. Unprenylated RAB27A accumulates in choroideremia patients; the cytosolic levels of RAB27A increased in RPE cells differentiated from hiPSCs derived from a choroideremia patient [28,29]. In addition to RAB27A, RAB38 has been suggested to contribute to choroideremia [30]. The cytosolic levels of RAB27A and RAB38 were significantly increased in CHM#1 RPE cells, probably reflecting REP-1 dysfunction (Fig. 4D). Although high RAB27A levels were also observed in CHM#1_sk6 RPE cells, the RAB38 level was significantly decreased (compared to that in CHM#1 RPE cells) (Fig. 4D). Thus, REP-1 lacking exon 6 may regulate the prenylation status of certain RABs, including RAB38, and the phagocytic activity of RPE cells.

Discussion

In this study, we sought to establish a platform by which non-specialized laboratories can evaluate whether gene therapy vectors repair mutations in RPE-expressed genes. Here, mutations that mimicked those of patients were introduced (using the CRISPR/Cas9 system) into hiPSCs. The host cells, those of the hOPM line, exhibit fast and efficient differentiation into RPE [15]. Experimental mutation of hOPM cells not only reduces the time required to establish hiPSC lines for each case but also allows the use of cells with identical genetic backgrounds, for comparison of the various vectors.

Several methods have been used to differentiate ESCs/iPSCs into RPE [9]. Accurate evaluation of differentiation of these methods is critical. While microscopic evaluation of hexagonal morphology and pigmentation (characteristic features of RPE cells) has been

employed, the *in vitro* manipulations associated with biochemical/molecular biological analyses are time-consuming and need to harvest cells. Furthermore, cells in tissue do not always differentiate homogeneously; any analysis of cell mixtures may yield inaccurate judgement. As a non-invasive reproducible test, combinations of quantitative bright-field absorbance microscopy with deep neural network (DNN) evaluations has been used to predict tissue function and the cellular donor identities of iPSC-derived RPE [31]. We have taken a similar approach to using an AI-based assay that can be implemented in many laboratories. We used photographs taken by a standard camera attached to a standard laboratory microscope without any lighting adjustment; AI accurately distinguished cells.

We evaluated how a *CHM* exon-skipping vector affected RPE cells with a frameshift mutation in *CHM* exon 6. RPE cells with a frameshift mutation in exon 6 did not exhibit any change (compared to normal cells) in terms of phagocytic activity or cell death Although choroideremia patients exhibit symptoms such as nyctalopia from the first decade of life, the disease progresses slowly and loss of central vision occurs only in the fifth-to-sixth decades [32]. Thus, eye changes on aging, perhaps created by increased oxidative stress, may play critical roles in disease progression.

The RAB family members orchestrate membrane trafficking; in particular, the RAB5 and RAB7 subfamily members are essential for phagosome maturation [33,34]. Although we found that *CHM* exon 6-skipping did not affect the overall level of RAB prenylation, changes in the prenylation levels of certain RABs may have been in play. RAB38 plays important roles in melanogenesis and ensures appropriate targeting of tyrosinase-related protein 1 to the melanosomes of RPE cells [35]. *Rab38*-deficient mice exhibited fewer and smaller mature melanosomes and a thinner RPE than did control mice [36]. *CHM* exon 6-skipping reduced the cytosolic RAB38 level; thus, the effects of *CHM* exon 6-skipping on melanosomes should be further explored.

The resolved structure of Rab7 in complex with REP-1 indicated that Rab binding platform, C-terminus binding region and helices D and E are crucial for the interaction among REP-1, Rab7 and RabGGTase [37] [38]. REP-1 lacking exon 6 loses a part of C-terminus biding region involved in the interaction with Rab7, while amino acids important for the interaction between REP-1 and RabGGTase remain in REP-1 lacking exon 6. Therefore, although REP-1 lacking exon 6 might show weaker interaction with RAB proteins, it is plausible that the interaction with RabGGTase remains unchanged, leading to the partially functional REP-1 protein. Compared with REP-1 lacking exon 6, REP-1 lacking exon 9 or 10 showed very low protein expression level, indicating exon 9 or 10 skipping largely decreased the REP-1 stability. A machine learning tool for the prediction of protein stability would give a rational explanation for this point [39].

In order to consider the off-target effect resulting from the CRISPR/Cas9 system, we made search of target sites by using CRISPRdirect (https://crispr.dbcls.jp/) with the following criteria: a sequence is matched with more than 12mer of 3' region of the target sequence adjacent to the PAM; a sequence is localized on a coding sequence. Genes *ETV4* and *OXSR1* are potential off-targets of gCHM_Ex6_01 and gCHM_Ex6SD, respectively. We performed sequence of these two genes with gCHM_Ex6_01 or gCHM_Ex6SD expressing

samples, and no mutation was identified. *CHML*, which encodes a homologous protein to *CHM*, was not included in the highly possible targets. Therefore, we concluded that the off-target effects are less plausible. We evaluated the effects of a *CHM* mutation and exon-skipping using only one clone, CHM#1. Although we performed preliminary experiments using transiently transfected cell population several times and obtained essentially the same results, we also cannot exclude the possible effects of clonal variation [40] on the phenotypes observed in this study. Thus, further analysis using choroideremia patient-derived hiPSCs would be valuable to assess the effects of *CHM* exon-skipping.

Most IRD mutations are recessive; patients are often compound heterozygotes. In such cases, alleles specific design of repair of the mutations is necessary if the mutations are in the different exons. Here, we designed gRNAs to target exon-SA and -SD sites. We previously constructed a plasmid contains tandem-two gRNAs, and this worked well [41]. The two gRNAs remove exons by targeting both ends of an intron. If single-nucleotide polymorphism (SNP) data are available, it is possible to target an SNP to one allele when designing an allele-specific exon-skipping vector; this would effectively and safely "cure" mutations. In summary, in this study, we showed that *CHM* exon-6 skipping partially rescued phenotypes appeared in RPE cells with a frameshift mutation in *CHM* exon 6 under oxidative stress probably by increasing RAB38 prenylation.

Supplementary Material

Refer to Web version on PubMed Central for supplementary material.

Acknowledgements

Data availability statement:

The data that support the findings of the present study are available from the corresponding author upon reasonable request.

References

1. Strauss O The retinal pigment epithelium in visual function. Physiol Rev. 2005;85(856–881).

2. Ferrari S, Di Iorio E, Barbaro V, Ponzin D, Sorrentino FS, Parmeggiani F. Retinitis pigmentosa: genes and disease mechanisms. Curr Genomics. 2011;12(4):238–249. doi:10.2174/138920211795860107 [PubMed: 22131869]

3. Guziewicz KE, Sinha D, Gómez NM, et al. Bestrophinopathy: An RPE-photoreceptor interface disease. Prog Retin Eye Res. 2017;58:70–88. doi:10.1016/j.preteyeres.2017.01.005 [PubMed: 28111324]

4. Prado DA, Acosta-Acero M, Maldonado RS. Gene therapy beyond luxturna: a new horizon of the treatment for inherited retinal disease. Curr Opin Ophthalmol. 2020;31:147–154. [PubMed: 32175942]

5. Miraldi Utz V, Coussa RG, Antaki F, Traboulsi EI. Gene therapy for RPE65-related retinal disease. Ophthalmic Genet. 2018;39(6):671–677. doi:10.1080/13816810.2018.1533027 [PubMed: 30335549]

6. Harrington EA, Sloan JL, Manoli I, et al. Neutralizing antibodies against adeno-associated viral capsids in patients with mut methylmalonic acidemia. Hum Gene Ther. 2016;27(5):345–353. doi:10.1089/hum.2015.092 [PubMed: 26790480]

7. Zarbin M, Sugino I, Townes-Anderson E. Concise Review: Update on Retinal Pigment Epithelium Transplantation for Age-Related Macular Degeneration. Stem Cells Transl Med. 2019;8(5):466–477. doi:10.1002/sctm.18-0282 [PubMed: 30748126]

8. Dalvi S, Galloway CA, Singh R. Pluripotent Stem Cells to Model Degenerative Retinal Diseases: The RPE Perspective. Adv Exp Med Biol. 2019;1186:1–31. doi:10.1007/978-3-030-28471-8_1 [PubMed: 31654384]

9. Leach LL, Clegg DO. Concise Review: Making Stem Cells Retinal: Methods for Deriving Retinal Pigment Epithelium and Implications for Patients With Ocular Disease. Stem Cells. 2015;33:2363–2373. [PubMed: 25809736]

10. Imani S, Ijaz I, Shasaltaneh MD, Fu S, Cheng J, Fu J. Molecular genetics characterization and homology modeling of the CHM gene mutation: A study on its association with choroideremia. Mutat Res Rev Mutat Res. 2018;775:39–50. doi:10.1016/j.mrrev.2018.02.001 [PubMed: 29555028]

11. Preising MN, Ayuso C. Rab escort protein 1 (REP1) in intracellular traffic: A functional and pathophysiological overview. Ophthalmic Genet. 2004;25(2):101–110. doi:10.1080/13816810490514333 [PubMed: 15370541]

12. Strunnikova NV, Barb J, Sergeev YV, et al. Loss-of-function mutations in rab escort protein 1 (REP-1) affect intracellular transport in fibroblasts and monocytes of choroideremia patients. PLoS One. 2009;4(12). doi:10.1371/journal.pone.0008402

13. DiCarlo JE, Mahajan VB, Tsang SH. Gene therapy and genome surgery in the retina. J Clin Invest. 2018;128(6):2177–2188. doi:10.1172/JCI120429 [PubMed: 29856367]

14. Amato A, Arrigo A, Aragona E, et al. Gene Therapy in Inherited Retinal Diseases: An Update on Current State of the Art. Front Med. 2021;8:750586. doi:10.3389/fmed.2021.750586

15. Dewell TE, Gjoni K, Liu AZ, et al. Transcription factor overexpression drives reliable differentiation of retinal pigment epithelium from human induced pluripotent stem cells. Stem Cell Res. 2021;53:102368. doi:10.1016/j.scr.2021.102368 [PubMed: 34087997]

16. Kreitzer FR, Salomonis N, Sheehan A, et al. A robust method to derive functional neural crest cells from human pluripotent stem cells. Am J Stem Cell. 2013;2:119–131.

17. Moriuchi Y, Iwagawa T, Tsuhako A, Koso H, Fujita Y, Watanabe S. RasV12 Expression in Microglia Initiates Retinal Inflammation and Induces Photoreceptor Degeneration. Invest Ophthalmol Vis Sci. 2020;61(13):34. doi:10.1167/iovs.61.13.34

18. Krohne TU, Stratmann NK, Kopitz J, Holz FG. Effects of lipid peroxidation products on lipofuscinogenesis and autophagy in human retinal pigment epithelial cells. Exp Eye Res. 2010;90(3):465–471. doi:10.1016/j.exer.2009.12.011 [PubMed: 20059996]

19. Klettner A, Möhle F, Lucius R, Roider J. Quantifying FITC-labeled latex beads opsonized with photoreceptor outer segment fragments: An easy and inexpensive method of investigating phagocytosis in retinal pigment epithelium cells. Ophthalmic Res. 2011;46(2):88–91. doi:10.1159/000323271 [PubMed: 21273797]

20. Almedawar S, Vafia K, Schreiter S, et al. MERTK-Dependent Ensheathment of Photoreceptor Outer Segments by Human Pluripotent Stem Cell-Derived Retinal Pigment Epithelium. Stem Cell Reports. 2020;14(3):374–389. doi:10.1016/j.stemcr.2020.02.004 [PubMed: 32160519]

21. Simonyan K, Zisserman A. Very deep convolutional networks for large-scale image recognition. 3rd Int Conf Learn Represent ICLR 2015 - Conf Track Proc. Published online 2015:1–14.

22. Russakovsky O, Deng J, Su H, et al. ImageNet Large Scale Visual Recognition Challenge. Int J Comput Vis. 2015;115(3):211–252. doi:10.1007/s11263-015-0816-y

23. Nguyen UT, Wu Y, Goodall A, Alexandrov K. Analysis of protein prenylation in vitro and in vivo using functionalized phosphoisoprenoids. Curr Protoc Protein Sci. 2010;Chapter 14:Unit14.3. doi:10.1002/0471140864.ps1403s62

24. Di Polo A, Farber DB. Rod photoreceptor-specific gene expression in human retinoblastoma cells. Proc Natl Acad Sci U S A. 1995;92(9):4016–4020. doi:10.1073/pnas.92.9.4016 [PubMed: 7732024]

25. Brinkman EK, Chen T, Amendola M, Van Steensel B. Easy quantitative assessment of genome editing by sequence trace decomposition. Nucleic Acids Res. 2014;42(22):1–8. doi:10.1093/nar/gku936 [PubMed: 24376271]

26. Kiuchi K, Yoshizawa K, Shikata N, Moriguchi K, Tsubura A. Morphologic characteristics of retinal degeneration induced by sodium iodate in mice. Curr Eye Res. 2002;25(6):373–379. doi:10.1076/ceyr.25.6.373.14227 [PubMed: 12789545]

27. Zhang XY, Ng TK, Brelén ME, et al. Continuous exposure to non-lethal doses of sodium iodate induces retinal pigment epithelial cell dysfunction. Sci Rep. 2016;6(November):1–13. doi:10.1038/srep37279 [PubMed: 28442746]

28. Cereso N, Pequignot MO, Robert L, et al. Proof of concept for AAV2/5-mediated gene therapy in iPSC-derived retinal pigment epithelium of a choroideremia patient. Mol Ther Methods Clin Dev. 2014;1:14011. doi:10.1038/mtm.2014.11 [PubMed: 26015956]

29. Duong TT, Vasireddy V, Ramachandran P, et al. Use of induced pluripotent stem cell models to probe the pathogenesis of Choroideremia and to develop a potential treatment. Stem Cell Res. 2018;27:140–150. doi:10.1016/j.scr.2018.01.009 [PubMed: 29414605]

30. Köhnke M, Delon C, Hastie ML, et al. Rab GTPase prenylation hierarchy and its potential role in choroideremia disease. PLoS One. 2013;8(12):e81758. doi:10.1371/journal.pone.0081758 [PubMed: 24358126]

31. Schaub NJ, Hotaling NA, Manescu P, et al. Deep learning predicts function of live retinal pigment epithelium from quantitative microscopy. J Clin Invest. 2020;130(2):1010–1023. doi:10.1172/JCI131187 [PubMed: 31714897]

32. Coussa RG, Kim J, Traboulsi EI. Choroideremia: Effect of age on visual acuity in patients and female carriers. Ophthalmic Genet. 2012;33(2):66–73. doi:10.3109/13816810.2011.623261 [PubMed: 22060191]

33. Flannagan RS, Jaumouillé V, Grinstein S. The cell biology of phagocytosis. Annu Rev Pathol Mech Dis. 2012;7:61–98. doi:10.1146/annurev-pathol-011811-132445

34. Kwon W, Freeman SA. Phagocytosis by the Retinal Pigment Epithelium: Recognition, Resolution, Recycling. Front Immunol. 2020;11(November):1–15. doi:10.3389/fimmu.2020.604205 [PubMed: 32038653]

35. Lopes VS, Wasmeier C, Seabra MC, Futter CE. Melanosome maturation defect in Rab38-deficient retinal pigment epithelium results in instability of immature melanosomes during transient melanogenesis. Mol Biol Cell. 2007;18(10):3914–3927. doi:10.1091/MBC.E07-03-0268 [PubMed: 17671165]

36. Brooks BP, Larson DM, Chan CC, et al. Analysis of ocular hypopigmentation in Rab38cht/cht mice. Investig Ophthalmol Vis Sci. 2007;48(9):3905–3913. doi:10.1167/iovs.06-1464 [PubMed: 17724166]

37. Rak A, Pylypenko O, Niculae A, Pyatkov K, Goody RS, Alexandrov K. Structure of the Rab7:REP-1 complex: Insights into the mechanism of Rab prenylation and choroideremia disease. Cell. 2004;117(6):749–760. doi:10.1016/j.cell.2004.05.017 [PubMed: 15186776]

38. Pylypenko O, Rak A, Reents R, et al. Structure of Rab Escort Protein-1 in Complex with Rab Geranylgeranyltransferase. Mol Cell. 2003;11(2):483–494. doi:10.1016/S1097-2765(03)00044-3 [PubMed: 12620235]

39. Yang Y, Ding X, Zhu G, Niroula A, Lv Q, Vihinen M. ProTstab - Predictor for cellular protein stability. BMC Genomics. 2019;20(1):1–9. doi:10.1186/s12864-019-6138-7 [PubMed: 30606130]

40. Onder TT, Daley GQ. New lessons learned from disease modeling with induced pluripotent stem cells. Curr Opin Genet Dev. 2012;22(5):500–508. doi:10.1016/j.gde.2012.05.005 [PubMed: 22749051]

41. Deng X, Iwagawa T, Fukushima M, Watanabe S. Characterization of human-induced pluripotent stem cells carrying homozygous RB1 gene deletion. Genes Cells. 2020;25(7):510–517. doi:10.1111/gtc.12771 [PubMed: 32277725]
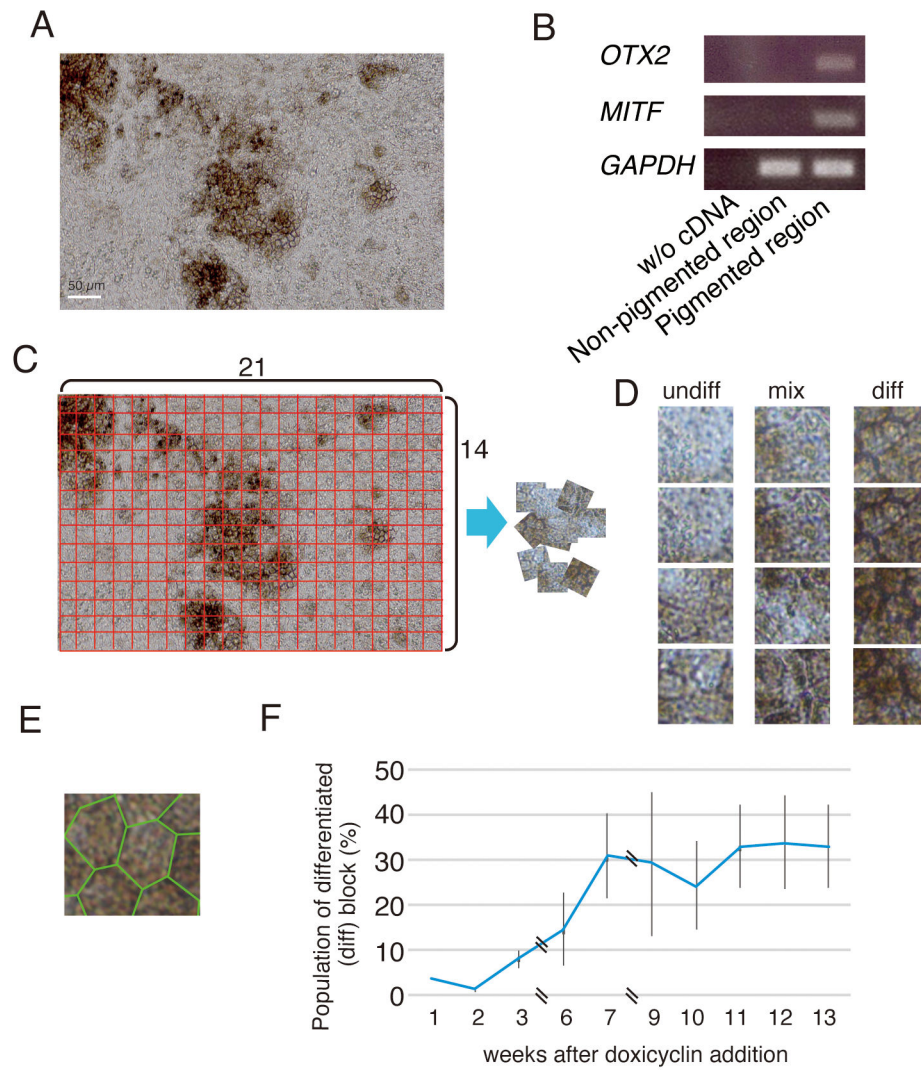
Figure 1. Preparation of materials to establish AI based evaluation of cell differentiation into RPE from WTC11

A. Representative photo of the culturing RPE from WTC11. Scale bar: 50 μm. B. The mRNA expression level of the cells in non-pigmented region or pigmented region. After 12-week of culture, the cells in each region were collected, and RT-PCR was performed. C. Total 294 squares are made from 1 photo. D. Representative examples of "undiff", "mix", and "diff" categorized squares. E. Green lines indicate that each diff block contains about 7–8 hexagonal cells. F. Population of "diff" categorized squares during RPE differentiation culture was calculated.
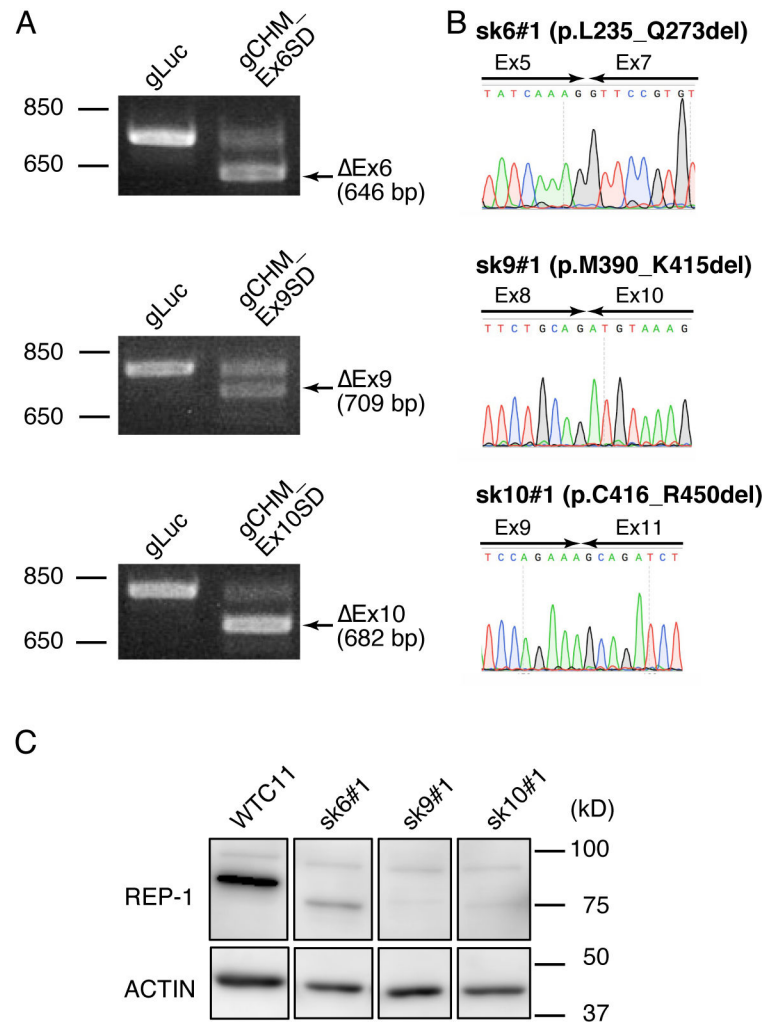
Figure 2. The induction of the *CHM* exon 6, 9, or 10 skipping and the expression of truncated REP-1 in hiPSC

A. The detection of the *CHM* exon 6, 9, or 10 skipping by RT-PCR. After electroporation of WTC11 with plasmids expressing gRNA, Cas9, and GFP, GFP-positive cells were sorted and cultured for 1 week. Total RNA was extracted, and RT-PCR was done. Each arrow indicates the PCR products derived from mRNA without the target exon. B. The sequences of PCR products without the target exons. Total RNA extracted from 3 clonal cell lines, sk6#1, sk9#1, and sk10#1, was used for RT-PCR. The PCR products derived from mRNA without the target exon was purified and sequenced. C. Western blotting to examine the expression of truncated REP-1. Whole cell lysate was extracted from WTC11 or 3 clonal cell lines, and Western blotting using anti-REP-1 or anti-ACTIN antibody was done. Molecular weight of exon 6, 9, and 10 was about 4.6, 2.9, and 4.2 kDa. Therefore, molecular weight of REP-1 without exon 6, 9, or 10 was estimated as 68.9, 70.6 or 69.3 kDa. Post-translational modification might increase the size of REP-1.
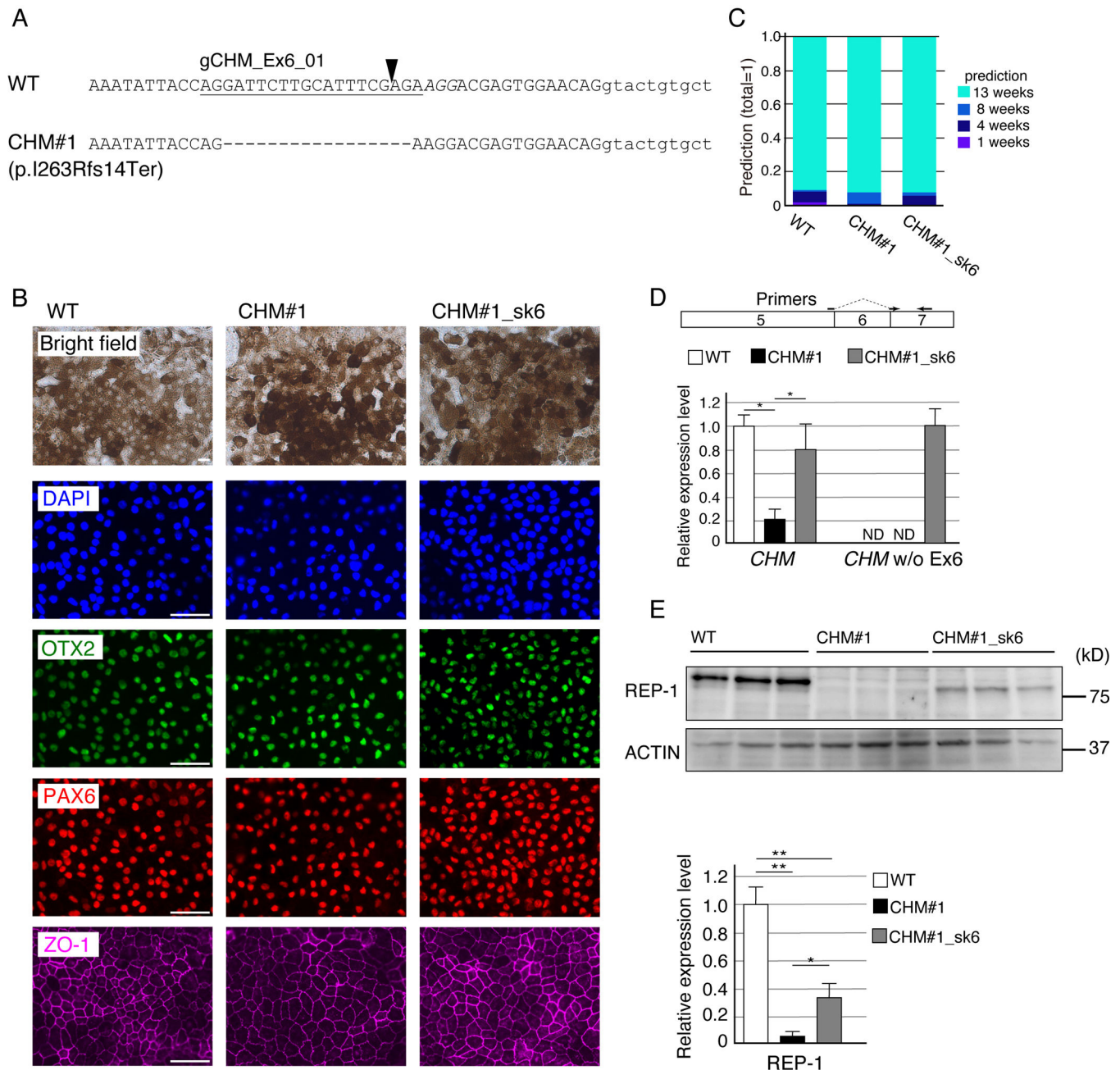
Figure 3. The differentiation of hOPM cell lines into RPE cells and the *CHM* mRNA and REP-1 expression

A. The sequence of the established clonal cell line with the frameshift mutation in the *CHM* exon 6 (CHM#1). CHM#1 has 17-nt deletions in the *CHM* exon 6, which leads to the appearance of a premature stop codon.

(B–E) Immunocytochemistry, AI-based staging analysis, RT-qPCR, and Western blotting of RPE cells 7 weeks after electroporation. hOPM or CHM#1 RPE cells were electroporated with plasmid expressing Cas9 and gLuc or gEx6SD and cultured for 7 weeks. B. Immunocytochemistry using anti-OTX2, PAX6, or ZO-1 antibody was carried out. Nuclei were stained with DAPI. C. The AI staging analysis. The RPE cells were categories into

4 stages. The y-axis indicates the percentage of each category. D. The results of RT-qPCR to examine the *CHM* mRNA expression level were shown. The primer set to detect *CHM* without exon 6 was shown above the results. Values are average of at least 3 independent samples with standard deviation. E. Western blotting results using anti-REP-1 and ACTIN are shown. The expression level of REP-1 was normalized to that of ACTIN. Average of 3 independent samples with standard deviation is shown. Scale bar: 50 μm. p*<0.05, ** <0.01 (Tukey's HSD test).
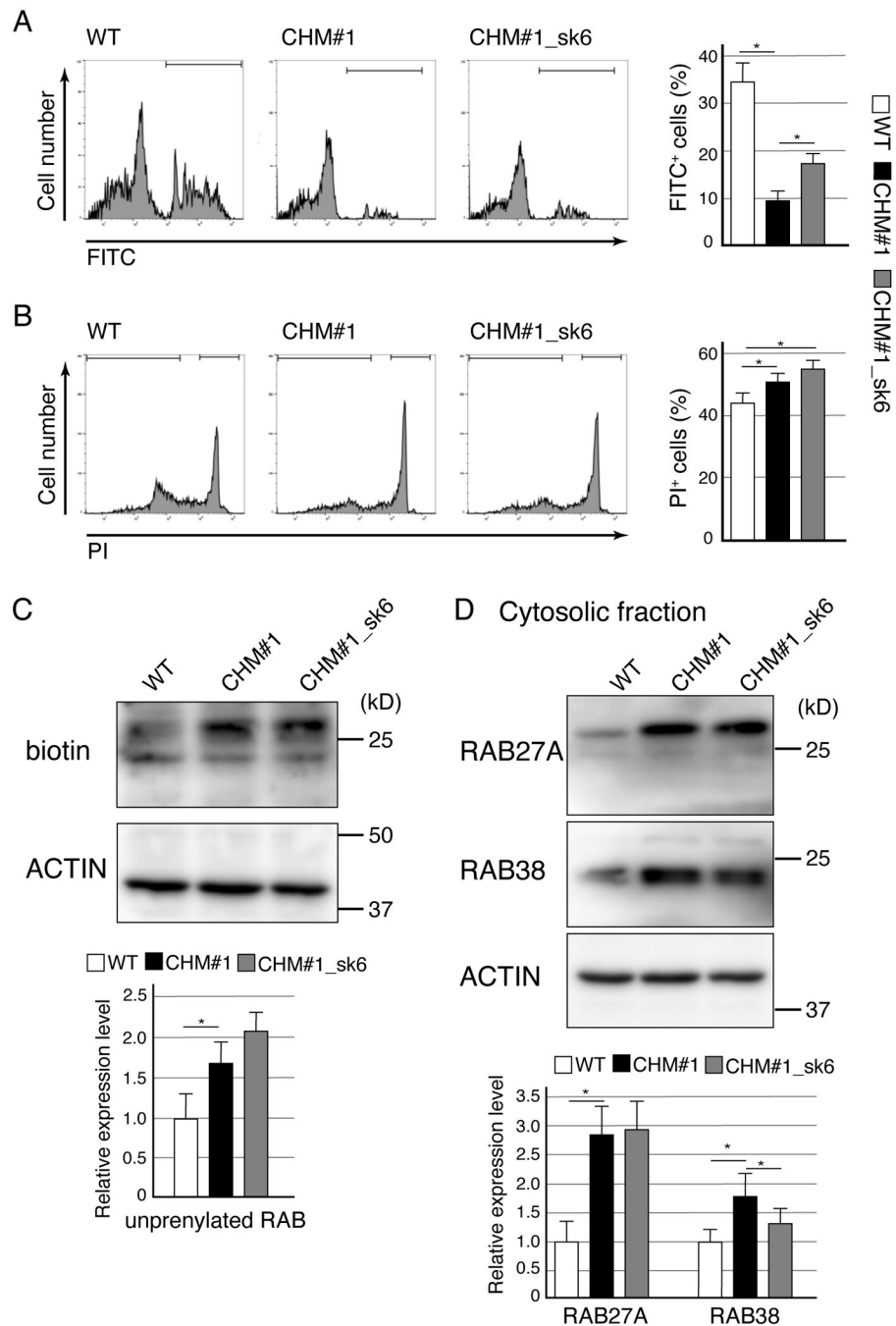
Figure 4. REP-1 without exon 6 contributed to the phagocytic activity of RPE cells under oxidative stress likely due to the effects on the localization of RAB38.

After 7 weeks differentiation, the hOPM or CHM#1 RPE cells were electroporated with plasmid expressing gLuc or gEx6SD and cultured for 7 weeks. The RPE cells were treated with 2 mM sodium iodate for 24 hours. A, B. Phagocytic activity using FITC-labeled latex beads opsonized with porcine POS and cell death using propidium iodide (PI) were examined by flow cytometry. In the left histograms, x-axis shows the fluorescence intensity of FITC or PI. In the right bar graphs, the percentage of FITC-positive or PI-positive cells is shown. Values are average of 3 independent samples with standard deviation. p*<0.05

(Tukey's HSD test). C. *In vitro* prenylation assay. Unprenylated RABs were labeled with biotin during *in vitro* prenylation reaction and detected by HRP-conjugated streptavidin. The relative signal intensity of biotin was normalized with that of ACTIN, and average of 3 independent samples with standard deviation is shown in the bar graph. $p^* < 0.05$ (Tukey's HSD test). D. The amount of RAB27A and RAB38 in the cytosolic fraction. The cytosolic fractions were collected by ultracentrifugation and the amount of indicated proteins was detected by Western blotting. The relative signal intensity of RAB27A and RAB38 was normalized with that of ACTIN, and average of 3 independent samples with standard deviation is shown in the bar graph. $p^* < 0.05$ (Tukey's HSD test).

Table 1

Cross-segregation of "diff", "mix", and "undiff" of squares obtained from photos at 4 and 5 weeks of the culture

predict \ true	undiff 483 block	mix 400 blocks	diff 587 blocks	All 1470 blocks
undiff	405	151	50	606
mix	54	122	80	256
diff	24	127	457	608
All	483	400	587	1470
accuracy	0.84	0.30	0.78	0.67

Table 2

Cross-segregation of "diff", "mix", and "undiff" of squares obtained from photos at 6 and 7weeks of the culture

predict \ true	undiff 624 blocks	mix 449 blocks	diff 597 blocks	All 1670 blocks
undiff	525	154	52	731
mix	73	203	134	410
diff	26	92	411	529
All	624	449	597	1670
accuracy	0.84	0.56	0.69	0.68

Table 3

Cross-segregation of "diff", "mix", and "undiff" of squares obtained from photos at 8 and 9 weeks of the culture

predict \ true	undiff 280 blocks	mix 378 blocks	diff 663 blocks	All 1321 blocks
undiff	239	90	1	330
mix	41	217	63	321
diff	0	71	599	670
All	280	378	663	1321
	0.85	0.57	0.90	0.80

Table 4

Cross-segregation of "diff" squares obtained from photos at 4 and 5 weeks vs 6 and 7 weeks vs 8 and 9 weeks of the culture

predict \ true	4/5 wks	6/7 wks	8/9 wks	All
4/5 wks	581	2	6	589
6/7 wks	3	595	0	598
8/9 wks	3	0	657	660
All	587	597	663	1847
accuracy	1.00	1.00	0.99	0.99

Table 5

Prediction of culture duration (weeks) of "diff" squares obtained from photos at 1, 4, 8 or 13 weeks of the culture by using the model

	Sample stage				
predict \ true	1 wk	4 wks	8 wks	13 wks	Total
1 wk	74	3	3	0	80
4 wks	0	326	0	4	330
8 wks	0	0	807	303	1110
13 wks	0	39	76	312	427
Total	74	368	886	619	1947
accuracy	1.0	0.886	0.911	0.504	0.780